

## Lifetime evaluation of three-phase multifunctional PV inverters with reactive power compensation



J.M.S. Callegari<sup>a</sup>, M.P. Silva<sup>b</sup>, R.C. de Barros<sup>a</sup>, E.M.S. Brito<sup>c</sup>, A.F. Cupertino<sup>c,d</sup>, H.A. Pereira<sup>b,\*</sup>

<sup>a</sup> Graduate Program in Electrical Engineering, Federal Center for Technological Education of Minas Gerais, Belo Horizonte, Brazil

<sup>b</sup> Department of Electrical Engineering, Federal University of Viçosa, Viçosa, MG, Brazil

<sup>c</sup> Graduate Program in Electrical Engineering, Federal University of Minas Gerais, Belo Horizonte, MG, Brazil

<sup>d</sup> Department of Materials Engineering, Federal Center for Technological Education of Minas Gerais, Belo Horizonte, Brazil

### ARTICLE INFO

#### Keywords:

Photovoltaic system  
Multifunctional inverter  
Reactive power injection  
Dynamic saturation  
Reliability  
Lifetime

### ABSTRACT

The multifunctional operation of photovoltaic inverters consists in providing ancillary services to the grid, such as reactive power injection, harmonic current compensation, frequency regulation and others. These extra activities can cause higher electro-thermo-mechanical stress in the inverter components, affecting their reliability. Hence, this work aims to analyze the multifunctional inverters reliability when the injection of a real industry reactive power profile is performed. The evaluation has been carried out on a grid-connected three phase photovoltaic system, considering a mission profile from Denmark. An equivalent thermal model is used to estimate the power devices junction temperature. Furthermore, a lifetime model applied to the Palmgren-Miner's rule is used to evaluate the inverter lifetime consumption. Afterward, a statistical analysis simulates several power devices operation scenarios, for the cases with and without reactive power injection. Finally, the results show that the reactive power injection has a considerable impact on the inverter reliability, reducing by 3 and 1.5 times the lifetime estimation when this service is performed without power restrictions and considering the dynamic power saturation, respectively.

### 1. Introduction

Renewable energy contributed with more than two-thirds of the world's new power capacity in 2017 (178 GW) [1]. In this scenario, the solar photovoltaic (PV) capacity grew by 50%, reaching over 74 GW installed. For the first time, the solar PV technology rose faster than any other source, surpassing coal net growth. Therefore, the PV systems are at work in the current energy market, with great potential to become one of the major energy sources in the near future [2].

PV systems attracted great interest for the production of sustainable electricity for diversified purposes. Besides, these systems present lower environmental impacts and reduced maintenance costs [3–5]. However, the increasing penetration of PV systems into the grid has made it more vulnerable, decentralized and susceptible to disturbances, which has led to the conductance of studies on their connection impacts [6].

An important issue involving the PV systems connection impacts into the grid is the reduction of the power factor (PF) of the consumer units that produce active power to supply their own energy demand. In this case, the reactive power ( $Q$ ) required by the load is only supplied

by the grid. According to the grid code requirements, the reduction of PF implies the application of fees by the electric utility, which reduces the economic advantage of PV systems [7]. Currently, two conventional techniques are used to solve this problem: synchronous machines and capacitor banks. The former provides reactive power to the system, when overexcited. It is economically viable in operations involving loads greater than 200 HP. Alternatively, the latter is used for localized reactive power compensation. However, switching a capacitor bank during a transient instability may not be fast enough to prevent damages to the system [8]. These limitations suggest the need for a new approach in order to improve flexibility and reduce costs.

Recently, the multifunctional PV inverter presents itself as a solution with high effectiveness for the aforementioned limitations [9], since its reactive power injection control allows the inverter to realize the PF correction and consequently the grid voltage regulation. Moreover, as the inverter is generally close to the consumer centers, it can provide reactive power to the loads, avoiding reactive current circulation in the transmission lines and reducing power losses as a consequence.

\* Corresponding author.

E-mail addresses: [jm\\_callegari@hotmail.com](mailto:jm_callegari@hotmail.com) (J.M.S. Callegari), [matheus.p.silva10@gmail.com](mailto:matheus.p.silva10@gmail.com) (M.P. Silva), [rodrigocdebarros@gmail.com](mailto:rodrigocdebarros@gmail.com) (R.C. de Barros), [erickk.brito@gmail.com](mailto:erickk.brito@gmail.com) (E.M.S. Brito), [afcupertino@ieee.org](mailto:afcupertino@ieee.org) (A.F. Cupertino), [heverton.pereira@ufv.br](mailto:heverton.pereira@ufv.br) (H.A. Pereira).

The extra work-time of the multifunctional operation by means of reactive power compensation can cause additional thermal stress, decreasing the inverter reliability. Previous studies show that PV inverters are among the least reliable components. According to [10], about 37% of the PV plants unexpected failures occur in the inverter. Reference [6] shows that about 32% of the inverter failures occur in the power semiconductors. In addition, the manufacturers of PV modules guarantee lifetime over 20 years, while the typical guarantee period for PV inverters ranges from 5 to 10 years [11].

Currently, studies on the multifunctional inverter have risen great interest from academic publications, mainly regarding the design, control and reliability areas. For example, reference [12] discusses the thermal control technique of the power device by means of the reactive power that circulates between parallel converters, improving devices reliability. Reference [13] studies the effects of reactive power injection from PV inverters on their lifetime. Besides, the author translates the reduction in inverter lifetime due to reactive power injection into reactive power cost for PV system. The impact of PV module characteristic on the PV inverters reliability and lifetime is approached by [14]. On the other hand, reference [15] analyzes the reliability based on a long-term thermal loading of the PV inverter with different values of reactive power injection at night or during low solar irradiance profile, according to the available inverter apparent power margin.

Despite the efforts of multifunctional PV inverter researchers, few works in literature analyze the effect of thermal stress on power modules, when the PV inverter injects reactive power. Furthermore, the reactive power profiles considered in these works are artificial. The industries are interested in evaluating the impacts of reactive power injection according to a real profile, which has not been investigated yet. Thus, this paper aims to fulfill this void in the literature, presenting a study on inverter lifetime when a real reactive profile obtained from an industry is injected. In view of the points aforementioned, this work provides the following contributions:

- Analysis of the impacts on the PV inverter injecting reactive power according to an industry reactive power profile;
  - Lifetime analysis with the Monte Carlo simulation for reactive power injection in comparison with the conventional operation.

This paper is outlined as follows: Section 2 provides the description of the modeling control strategy implemented to regulate the active and reactive power flow. Section 3 introduces the PV inverter thermal modeling. Moreover, in Section 4, it is presented the methodology to study the lifetime analysis of the three-phase grid-connected PV inverter power devices. Section 5 presents a case study with and without reactive power compensation, determining the lifetime consumption as a result. The inverter reliability, considering the dynamic saturation, is also evaluated. Conclusions are stated in Section 6.

## 2. Control strategy and system parameters

The PV system considered in this paper has a grid-connected three phase configuration, as shown in Fig. 1(a). The inverter is connected to the grid through a LCL filter, which reduces the current harmonics [16,15].

The control algorithm is implemented in synchronous reference frame (dq) developed in two loops, as shown in Fig. 1(b). The inner loop has a faster dynamic response and controls the current injected by the inverter. The outer loop is slower and controls the reactive power injection and dc-link voltage [17]. A Synchronous Reference Frame Phase-Locked Loop (SRF-PLL) structure is used to synchronize the inverter output with the grid [18]. Moreover, anti-windup PI controllers are used. Finally, the Space Vector (SV) modulation strategy is applied. The system parameters are given in Table 1.

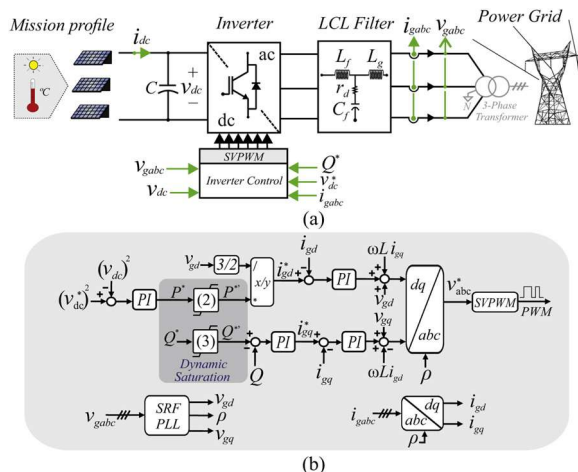


**Fig. 1.** (a) Structure of a three-phase grid-connected PV system. (b) Control strategy block diagram, considering the dynamic power saturation concept.

**Table 1**  
Parameters of the PV system

Parameter	Label	Value
Rated apparent power	$S_n$	8 kVA
Rated rms grid voltage	$V_g$	380 V
Rated grid phase current amplitude	$I_{cm}$	17.19 A
DC-link voltage	$v_{dc}$	630 V
Nominal grid angular frequency	$\omega_n$	377 rad/s
Nominal grid frequency	$f_n$	60 Hz
DC-link capacitor	$C_{dc}$	1.5 mF
Filter inductance	$L_g$	0.86 mH
Filter inductance	$L_f$	0.86 mH
Filter capacitance	$C_f$	3.7 $\mu$ F
Filter damping resistor	$r_d$	1 $\Omega$
Switching frequency	$f_{sw}$	12 kHz

### 2.1. Active and reactive power injection control

The active power injection is controlled by the direct-axis ( $d$ ) current  $i_{gd}$  and the reactive power ( $Q$ ) injection, by the quadrature-axis ( $q$ ) current  $i_{gq}$  in the inner loop, as shown in Fig. 1(b). This fact can be explained by the action of SRF-PLL, whose  $v_{gq}$  at the measurement point is zero. Therefore the expression of  $Q$  injected to the grid is expressed by,

$$Q = \frac{3}{2}(v_{\text{gg}} i_{\text{gd}} - v_{\text{gd}} i_{\text{gg}}) = -\frac{3}{2}(v_{\text{gd}} i_{\text{gg}}), \quad (1)$$

where  $v_{gd}$  and  $i_{gq}$  are the direct grid voltage and the quadrature grid current, respectively. Notably, without reactive compensation, the current  $i_{ga}$  is zero.

Two inverter operating conditions are considered: total reactive power injection, according to the load requirements; and reactive power injection, determined by the dynamic power saturation, as shown in Fig. 1(b). The worst case occurs at the first analysis, where the inverter can exceed its current margin and works overloaded.

The second approach performs the dynamic power saturation, providing total or partial reactive power compensation based on the inverter apparent power margin. The priority is the active power injection. If there is still a power margin, the inverter injects the reactive power required by the load.

The procedure initially consists of saturating the active power reference  $P^*$  with the rated apparent power, resulting in  $P^{*'}$  given by:

$$|P^{*'}| \leq S_n. \quad (2)$$

Afterward, the reactive power reference  $Q^*$  is calculated, considering  $S_n$  and  $P^*$ :

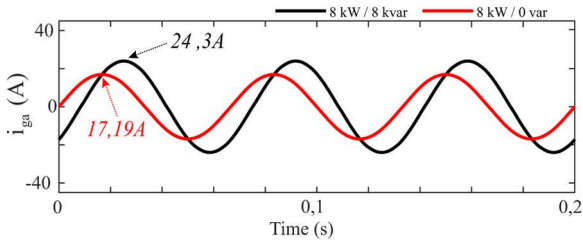


Fig. 2. Phase current injected into the grid with and without reactive power injection.

$$|Q^*| \leq \sqrt{S_n^2 - P^{*2}}. \quad (3)$$

If the vector sum of  $P^{*}$  and  $Q^*$  results in an apparent power smaller than the rated one, the reactive power compensation is total. Otherwise, reactive power compensation is partial.

## 2.2. Power losses analysis in electronic devices with reactive power injection

Under perfectly balanced conditions and disregarding the effect of the switching harmonics, the apparent power  $S$  injected into the grid increases according to the compensated reactive power, as demonstrated by:

$$S = \sqrt{P^2 + Q^2} = \sqrt{3} V_g I_g, \quad (4)$$

where  $I_g$  and  $V_g$  are the *rms* values of the grid current and voltage, respectively. Considering the grid as an infinite bus, an increase of apparent power means a higher injected current  $I_g$ . These results are presented in Fig. 2 for two cases: with 8 kvar and zero  $Q$  injection.

The amplitude of the current increases by 41.42% when 8 kvar is injected into the grid. In addition, the currents with and without  $Q$  compensation are not in phase, reducing the PF. The operation under non unitary condition can directly impact the thermal loading in the inverter semiconductor devices, e.g., diode and IGBT. Thus, the relationship between apparent power injection and power losses must be evaluated analytically at first. The total power losses ( $P_{tot}$ ) on power modules is described as a sum of switching and conduction losses, as follows:

$$P_{tot} = P_c + P_{sw}, \quad (5)$$

where  $P_c$  and  $P_{sw}$  refer to the sum of IGBT and diode conduction and switching power losses, respectively. The IGBT and diode conduction power losses are modeled considering that the current and voltage waveforms are displaced by an angle  $\theta$ . The current and voltage of the phase  $a$  at the inverter output are defined by:

$$i_{ga} = I_{cm} \sin(\alpha), \quad (6)$$

$$v_{ga} = V_{cm} \sin(\alpha + \theta), \quad (7)$$

where  $\alpha = \omega_n t$ ,  $I_{cm}$  is the phase current amplitude and  $V_{cm}$  is the phase voltage amplitude. Besides, the typical collector-emitter voltage  $v_{ce}$  and collector current  $i_c$  of the IGBT can be approximated by a linear equation in its operating range, as well as the forward voltage  $v_f$  and forward current  $i_f$  of the diode, as shown in (8) and (9) [19]:

$$v_{ce} = \left( \frac{V_{cen} - V_{ce0}}{I_{cn}} \right) i_c + V_{ce0} = r_i i_c + V_{ce0}, \quad (8)$$

$$v_f = \left( \frac{V_{fn} - V_{f0}}{I_{cn}} \right) i_c + V_{f0} = r_{di} i_c + V_{f0}, \quad (9)$$

where  $V_{cen}$ ,  $V_{ce0}$ ,  $V_{fn}$ ,  $V_{f0}$ ,  $I_{cn}$ ,  $r_i$  and  $r_{di}$  are collector-emitter voltage for rated operating condition, IGBT on-state zero current collector-emitter voltage, forward diode voltage for rated condition, on-state zero current voltage across the diode, rated collector current, collector-emitter on-state resistance and diode on-state resistance, respectively. All these

parameters are easily found on component manufacturers' datasheets.

In [20], the authors show that the conduction losses for SVPWM may be computed in the same way as a sine-triangular PWM (SPWM), representing a good approximation. However, for a more accurate approach, it is considered the insertion of zero sequence components (odd harmonics multiples of 3) in the sine modulation function  $h(\alpha + \theta)$  [19], as follows:

$$h(\alpha + \theta) = \sin(\alpha + \theta) + \frac{1}{6} \sin[3(\alpha + \theta)]. \quad (10)$$

The duty cycle  $\delta$  of the voltage pulses is obtained by comparing the modulation signal (10) with the carrier signal, given by:

$$\delta = \frac{1}{2} [1 + mh(\alpha + \theta)], \quad (11)$$

where  $m = \sqrt{3} V_{cm}/v_{dc}$  is the modulation index. It is possible to express the IGBT current as the product of the inverter output current and the duty cycle (11). Thus, the IGBT conduction losses  $P_{c,I}$  are calculated by [20]:

$$P_{c,I} = \frac{1}{2\pi} \int_0^\pi v_{ce} i_c \delta d\alpha. \quad (12)$$

Similarly, the diode conduction losses  $P_{c,D}$  are given by:

$$P_{c,D} = \frac{1}{2\pi} \int_0^\pi v_{ce} i_c (1 - \delta) d\alpha. \quad (13)$$

After solving (12) and (13) and applying several math manipulations, the results obtained for IGBT and diode are given by (14) and (15), respectively:

$$P_{c,I} = \left[ \frac{1}{8} + \frac{m}{3\pi} \cos(\theta) - \frac{m}{30\pi} \cos(3\theta) \right] I_{cm}^2 r_i + \left[ \frac{1}{2\pi} + \frac{m}{8} \cos(\theta) \right] V_{ce0} I_{cm}, \quad (14)$$

$$P_{c,D} = \left[ \frac{1}{8} - \frac{m}{3\pi} \cos(\theta) + \frac{m}{30\pi} \cos(3\theta) \right] I_{cm}^2 r_{di} + \left[ \frac{1}{2\pi} - \frac{m}{8} \cos(\theta) \right] V_{f0} I_{cm}. \quad (15)$$

In contrast to the conduction losses, the switching losses do not directly depend on the modulation function [20]. The energy required to switch the IGBT is presented as graphs in the datasheets provided by the device manufacturer. Reference [19] analyzes a typical switching curve of an IGBT, approaching some parameters to simplify the calculations. The average switching power losses, described by the sum of turn-on switching losses  $P_{on,I}$  and turn-off switching losses  $P_{off,I}$ , follow the methodology applied in [19], where the angle  $\theta$  between voltage and current is considered. They are given by (16) and (17):

$$P_{on,I} = \frac{f_{sw} v_{dc}}{2\pi} \left[ \frac{\pi I_{cm}^2 t_{rn}}{4I_{cn}} + 2Q_{rn} \left( 0.28\pi + 0.38 \frac{I_{cm}}{I_{cn}} + 0.015\pi \frac{I_{cm}^2}{I_{cn}^2} \right) + \left( 1.6I_{cm} + 0.1\pi \frac{I_{cm}^2}{I_{cn}} \right) t_{rn} \right]. \quad (16)$$

$$P_{off,I} = \frac{f_{sw} v_{dc} I_{cm} t_{fn}}{2\pi} \left( \frac{2}{3} + \frac{\pi I_{cm}}{12I_{cn}} \right), \quad (17)$$

where  $I_{cn}$  gives the IGBT rated collector current,  $t_{rn}$  is the rated IGBT current rise time,  $Q_{rn}$  is nominal reverse diode recovery load,  $t_{rn}$  is the diode nominal reverse recovery time and  $t_{fn}$  is the rated IGBT current fall time. Finally, the IGBT total switching losses is the sum of  $P_{on,I}$  and  $P_{off,I}$ .

The turn-on switching energy of diodes is usually negligible [4], while the turn-off switching losses ( $P_{off,D}$ ) can be approximated by [19]:

$$P_{off,D} = \frac{f_{sw} v_{dc} Q_{rrn}}{2\pi} \left[ 0.28\pi + 0.38 \frac{I_{cm}}{I_{cn}} \right]. \quad (18)$$

**Table 2**

Typical values of the parameters from power losses equations found in the IGBT and diode datasheets.

Parameter	Label	Value
IGBT collector-emitter voltage	$V_{cen}$	2 V
IGBT on-state collector-emitter voltage	$V_{ceo}$	0.8 V
IGBT rated collector current	$I_{cn}$	25 A
Forward diode voltage	$V_{fn}$	1.7 V
On-state diode voltage	$V_{fo}$	0.5 V
Rated IGBT current rise time	$t_{fr}$	30 ns
Rated IGBT current fall time	$t_{fr}$	70 ns
Diode reverse recovery time	$t_{rr}$	200 ns
Diode reverse recovery load	$Q_{rr}$	2.3 $\mu$ C

Eqs. (14)–(18) demonstrate that the conduction power losses strongly depend on  $\theta$ , while the switching power losses are not influenced by  $\theta$ . Table 2 presents the typical values used to obtain the power losses curves in Fig. 3.

Although the proposed model does not show variations of the switching power losses with  $\theta$ , it should be clear that small variations in these power losses are noticed for an experimental study, since there are fluctuations in the dc-link voltage, distortions in the grid current and others, which were not considered to obtain the above equations.

Fig. 3(a) shows the conduction losses for variations of  $\theta$  when the converter injects fixed 8 kVA with different modulation indexes (0.70–1). When  $0 < |\theta| < \pi/2$ , the converter operates as an inverter and, if  $\pi/2 < |\theta| < \pi$ , the converter operates as a rectifier. Fig. 3(b) shows the switching power losses with  $\theta$  variation.

Regarding the power devices, the IGBT presents higher power losses than the diode during the inverter operation mode. In addition, the maximum power losses occur when  $\theta = 0$ , i.e. PF is unitary. On the other hand, diode conduction losses increase considerably when the reactive power injection increases. Furthermore, the diode greatest stress occurs in the rectifier region, which is not explored in PV inverters. The IGBT conduction power losses tend to reduce when the inverter operates under  $PF < 1$ , regardless of whether the FP is inductive or capacitive.

Another interesting fact is the low sensitivity of the diode reverse recovery losses and the IGBT switching power losses with the operating PF variation. Despite some peculiarities observed in the switching losses, the  $Q$  injection affects the semiconductor devices dynamics.

### 3. Thermal modeling of PV inverter

There are two IGBT packaging methods: press-pack packaging and module packaging. For historical reasons, the second method is widely used due to its lower cost, simpler maintenance and mounting. However, the power module has large thermal resistance due to soldering and bond wire of internal chips. As a consequence, higher thermal stresses in the module layers are observed, which impacts its failure rate [21,6].

The structure of a common IGBT module is composed of several layers of different materials, as shown in Fig. 4.  $Z_{th(jc)}$  refers to the

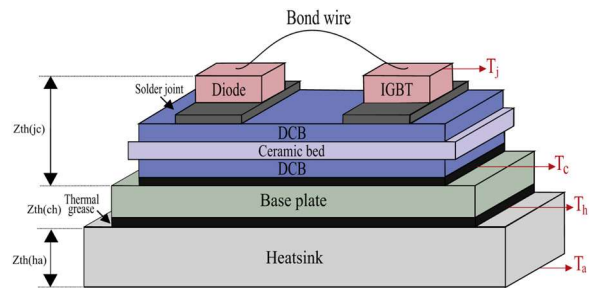


Fig. 4. Structure of a standard IGBT module.

transient thermal impedance between the junction of the IGBT chips and the case module,  $Z_{th(ch)}$  refers to the thermal impedance between case module and heatsink and  $Z_{th(ha)}$  is the transient thermal impedance between heatsink and ambient.

Generally, there are three main wear-out failure mechanisms on the IGBT modules due to cyclic thermal stress: the bond wire lift-off, solder joints cracking under the chip (diode and IGBT) and solder joints cracking under the direct copper-bonded (DCB) [22]. In this work, the bond wire failure is treated due to thermal cycling.

Regarding the PV inverter design, it was selected a 1200 V/25 A IGBT, with part number IKW25T120 manufactured by Infineon. In addition, the heatsink is designed to achieve an average junction temperature of 100 °C at the rated conditions of the PV inverter without reactive power compensation, for safety operation reasons. The thermal parameters are presented in Table 3.

### 4. Lifetime evaluation procedure

The mission profile of solar irradiance ( $G$ ) and ambient temperature ( $T_a$ ) are obtained from Aalborg, Denmark. Besides, the reactive power profile is obtained from a real food industry. This profile is sampled at one second with one year duration, as shown in Fig. 5.

Knowledge about the PV inverter operating conditions is essential in the lifetime study [2,23,24]. The mission profile has a strong impact on the PV system reliability. In order to obtain the junction temperature  $T_j$  of the power modules, the mission profile must be translated into a thermal loading [25].

Fig. 6 shows the main steps to translate the profiles into thermal loading. The active power  $P_{in}$  is obtained from the PV system model considering the mission profile as input [26]. For the power injection conditions, the switching devices are subject to thermal stress caused by conduction and switching power losses. The calculation of the total power losses is implemented with a look-up table, obtained from a certain set of operating conditions: reactive and active power injection as well as junction temperature. In this way, the losses under other conditions given by the mission profiles can be interpolated from the look-up table.

With the value of the power losses  $P_{loss}$ , it is possible to obtain the power devices junction temperature, considering the thermal model presented in Fig. 7 [23]. This is an electro-thermal model based on the Cauer's equivalent circuit to estimate the case temperature  $T_c$  and feed

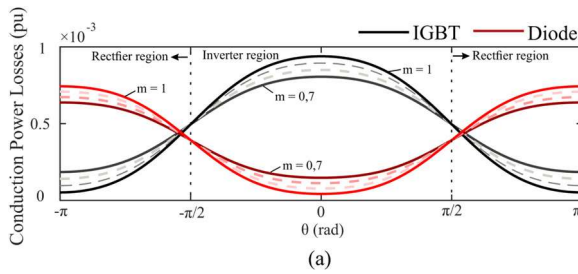
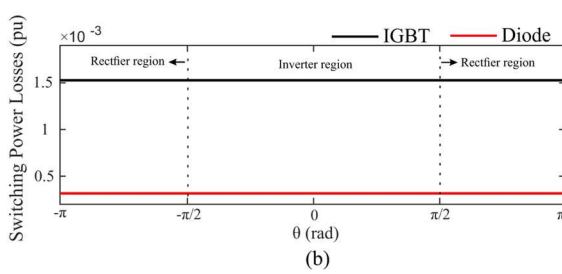
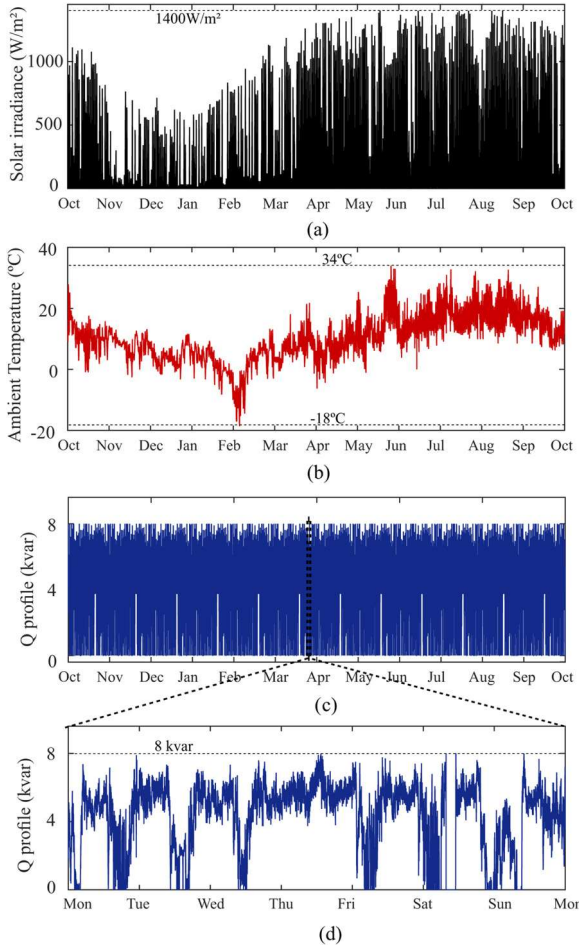


Fig. 3. Analysis of (a) conduction power losses and (b) switching power losses, for variations of  $\theta$  from  $-\pi$  to  $\pi$  and  $S_{base} = 8$  kVA.



**Table 3**  
Foster thermal impedance for IKW25T120 power module from Infineon.

Thermal impedance	$Z_{th(jc)}$				
		1	2	3	4
IGBT	$R$ (K/W)	0.229	0.192	0.174	0.055
	$\tau$ (s)	0.11	0.0156	0.00135	0.00015
Diode	$R$ (K/W)	0.282	0.317	0.294	0.107
	$\tau$ (s)	0.101	0.0115	0.0013	0.00015



**Fig. 5.** Mission profile of (a) solar irradiance 1-year profile, (b) ambient temperature 1-year profile, (c) reactive power injection 1-year profile, according to the load requirement and (d) zoom of reactive power injection 1-week profile.

it into the Foster's equivalent circuit, in order to obtain a better estimate of  $T_j$ .

#### 4.1. Lifetime evaluation for different time constants

The use of lifetime models requires three factors that directly affect the degradation of semiconductor devices, such as: heating time during the cycling period  $t_{on}$ , mean junction temperature  $T_{jm}$  and junction temperature fluctuation  $\Delta T_j$ . It is important to note that the thermal stresses in the power devices present different behaviors, according to two time constants [23]: (1) thermal cycling due to climatic variations (referred to as long-term) and (2) thermal cycling due to grid frequency (referred to as short-term).

Fig. 6 shows that the long-term time constant (with index  $l$ ) does not have well-defined thermal cycles. This is explained by an irregular profile, due to the mission profile dynamics [24]. Thus, a counting

algorithm (e.g. rainflow algorithm) is employed in order to find these thermal cycles. It allows obtaining the three parameters described above, which are applied to the lifetime model.

The short-term time constant (represented with index  $s$ ) has well-defined thermal cycles caused by the grid frequency oscillations. Thus,  $t_{on(s)} = 1/(2f_n)$  [23]. Therefore, it is not necessary to use thermal cycling counting algorithms in this case [23]. The junction temperature obtained from the equivalent thermal model is the mean junction temperature  $T_{jm(s)}$  and can be directly applied into the lifetime model. In addition, the junction temperature fluctuation  $\Delta T_{js}$  caused by the grid frequency can be analytically determined by [23,24]:

$$\Delta T_{js} = P_{loss} Z_{th} \left( \frac{3}{8f_n} \right) + 2P_{loss} Z_{th} \left( \frac{1}{4f_n} \right), \quad (19)$$

where  $Z_{th}$  is a time-based expression of device thermal impedance, which can be found in the component datasheet. The number of cycles to failure  $N_f$  is estimated by the Bayerer lifetime model proposed by [27]:

$$N_f(l,s) = A \Delta T_{j(l,s)}^{\beta_1} \exp \left( \frac{\beta_2}{T_{jm(l,s)} + 273} \right) t_{on}^{\beta_3} I^{\beta_4} V^{\beta_5} D^{\beta_6}, \quad (20)$$

where  $A$  and  $\beta$  coefficients are obtained via accelerated thermal tests.  $I$  is the current per bond foot,  $V$  is related to the blocking voltage and  $D$  is the bond wire diameter. This equation can be applied to both time constants and is used to quantify the wear-out bond wire lift-off due to thermo-mechanical stress. In addition, long-term analysis is carried out by limiting thermal cycles in the range of 1–15 s, according to the parameters defined in Table 4.

Since (20) is defined to  $t_{on}$  from 1 to 15 s, the estimated number of cycles for short-term analysis  $N_{f(s)}$  may be incorrect. Reference [28] shows the dependence of  $N_{f(s)}$  =  $f(t_{on})$ , given by:

$$\frac{N_{f(s)}(t_{on})}{N_{f(s)}(1.5\text{s})} = \left( \frac{t_{on}}{1.5\text{s}} \right)^{-0.3}, \quad 0.1 < t_{on} < 60\text{s}. \quad (21)$$

Thus,  $N_{f(s)}$  is calculated using (21), which expands the model validity range within  $0.1 < t_{on} < 60$  s. Although the heating time for the real application is not in the range of (21), it is the best approach found in the literature.

#### 4.2. Lifetime consumption evaluation

The total 1-year lifetime consumption ( $LC$ ) is a cumulative sum of the thermal cycle contributions due to the grid fundamental frequency (short-term) and climatic variations (long-term), represented by (22). As the grid frequency is  $f_n = 60$  Hz and the data is sampled at  $T_s = 1$  s, there are  $f_n \times T_s$  cycles per sample to be counted in the short-term contribution.

$$LC = \sum_k \left( \overbrace{\frac{1}{N_{f(l)k}}}^{\text{long-term}} + \overbrace{\frac{T_s f_n}{N_{f(s)k}}}^{\text{short-term}} \right). \quad (22)$$

#### 4.3. Monte Carlo reliability analysis

The total LC for one year is considered under a specific profile and it is understood that all the power devices will fail at the same time. However, depending of the manufacturing process and thermal stresses, the power devices can fail at different times due to uncertainties in the device parameter variations and the statistical properties of the applied lifetime model [6]. Therefore, a statistical analysis based on Monte Carlo simulation is performed, as illustrated in Fig. 8 [29,30].

In the first step, the stochastic and dynamic parameters of  $\Delta T_j$ ,  $t_{on}$  and  $T_{jm}$  have to be converted into equivalent deterministic and static ones, i.e.,  $\Delta T'_j$ ,  $t'_{on}$  and  $T'_{jm}$  [2]. The main goal is obtaining the

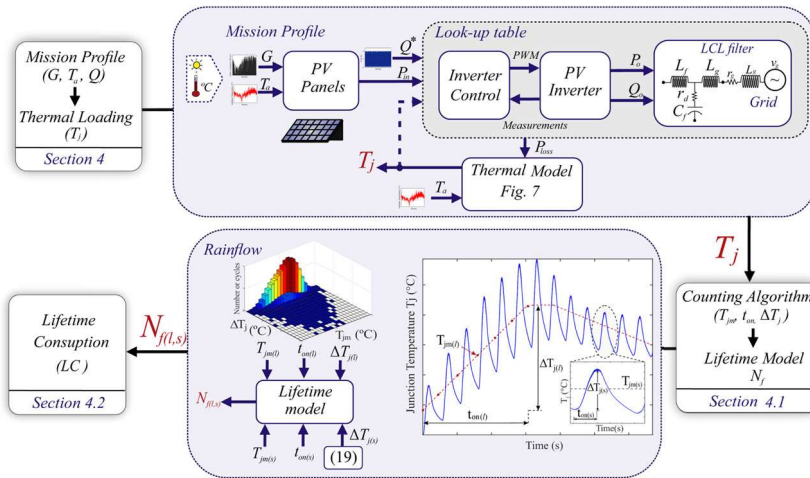


Fig. 6. Flowchart for the lifetime evaluation of power devices.

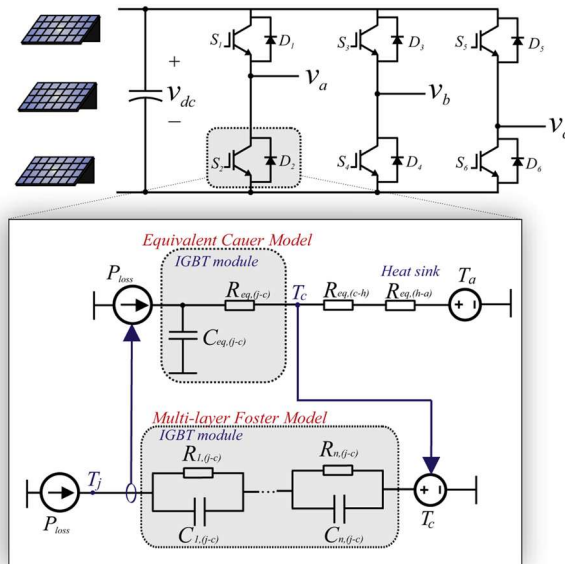
Fig. 7. Thermal model to estimate junction temperature.  
Adapted from [23].

Table 4

Parameters and limits for the calculation of  $N_f$  based on the Bayerer Model [27].

Parameter	Label	Limits	Coef.	Value
Technology factor	A	–	–	$9.34 \times 10^{14}$
Temp. fluctuation	$\Delta T_j$	45–150 °C	$\beta_1$	-4.416
Min. junction temp.	$T_{j,min}$	20–120 °C	$\beta_2$	1285
Cycling period	$t_{on}$	1–15 s	$\beta_3$	-0.463
Current per bond foot	I	3–23 A	$\beta_4$	-0.716
Blocking voltage	V	6–33 V	$\beta_5$	-0.761
Bond wire diameter	D	75–500 µm	$\beta_6$	-0.5

parameters which provide the same LC calculated in (22). Reference [2] suggests using  $T'_{jm}$  equal to the mean value of the junction temperature  $T_j$  and  $t'_{on} = 1/(2f_n)$  to reduce the number of degrees of freedom, since it is the most stressful heating time in the power devices.

By setting  $t'_{on}$ , it is possible to calculate the number of cycles of the device per year as  $NC' = 365 \times 24 \times 60 \times 60 \times 60$ . In addition, with the LC value, it is possible to determine  $N'_f$  by means of the Palmgren-Miner's rule:

$$LC = \frac{NC'}{N'_f}. \quad (23)$$

Finally, the equivalent static junction temperature fluctuation  $\Delta T'_j$  is obtained by applying (20) using the defined deterministic parameters:

$$\Delta T'_j = \sqrt[k]{\frac{N'_f}{k \exp\left(\frac{\beta_2}{T'_{jm} + 273}\right) t'^{\beta_3}_{on}}}, \quad (24)$$

where  $k = A I^{\beta_4} V^{\beta_5} D^{\beta_6}$ . Once the equivalent static values are obtained, a variation of 5% is applied in these parameters and in all the coefficients of Table 4. Afterwards, a Monte Carlo simulation is performed with a population of 10,000 samples.

The Monte Carlo simulation output values can be arranged in a histogram. The distribution of the power devices lifetime generally follows a Weibull function  $f(x)$  [31] defined as:

$$f(x) = \frac{\beta}{\eta^\beta} x^{\beta-1} \exp\left[-\left(\frac{x}{\eta}\right)^\beta\right], \quad (25)$$

where  $\eta$  is the scale parameter,  $\beta$  is the shape parameter and  $x$  is the operation time. Therefore, it is possible to fit the Probability Density Function (PDF)  $f(x)$  in the histogram generated with the  $n = 10,000$  samples [30].

Finally, the reliability of one power device can be evaluated by considering the Cumulative Density Function (CDF)  $F(x)$  of the Weibull distribution, given by the PDF area, as:

$$F(x) = \int_0^x f(x) dx. \quad (26)$$

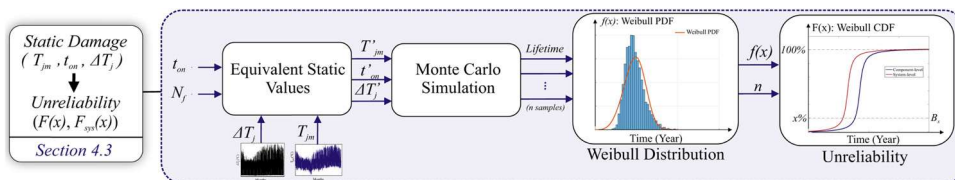
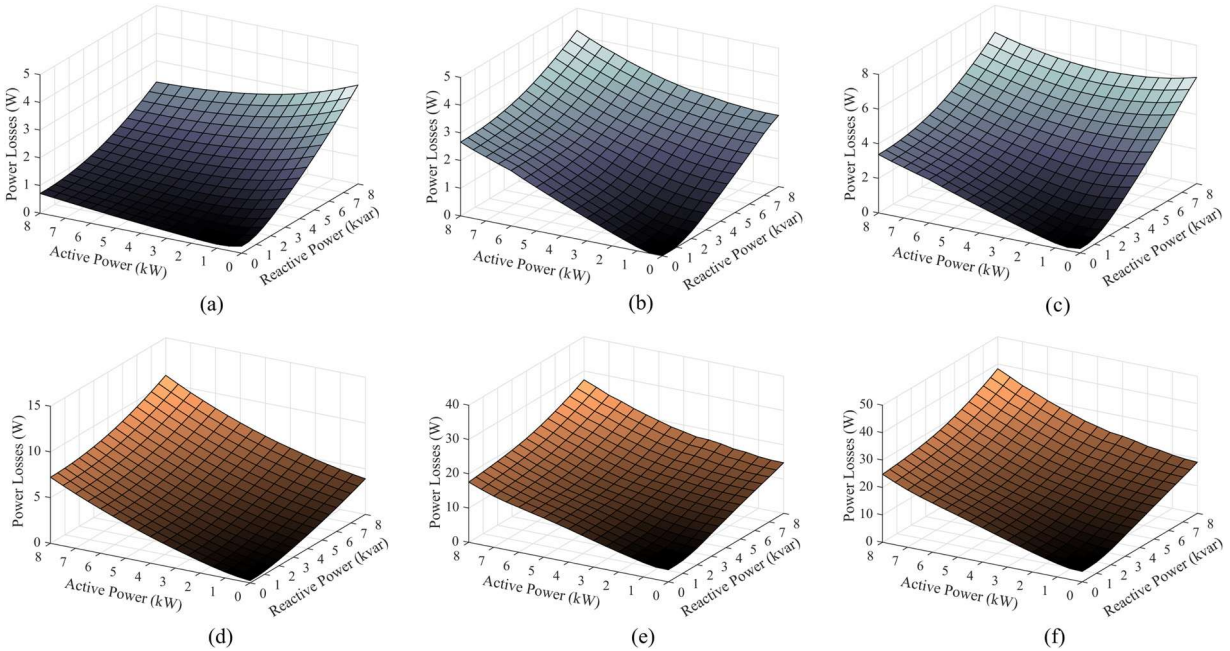


Fig. 8. Flowchart of the Monte Carlo reliability analysis.



**Fig. 9.** Power losses in the semiconductors devices considering different injections of active and reactive power. Diode: (a) conduction losses, (b) switching losses, and (c) total losses. IGBT: (d) conduction losses, (e) switching losses, and (f) total losses.

$F(x)$  is called unreliability function. In addition, from  $F(x)$  it is possible to obtain the lifetime  $B_x$ , which refers to the time when  $x\%$  of samples have failed [30].  $B_{10}$  is common reliability metric used by manufacturers and reliability project engineers.

With the Monte Carlo analysis, the power device failure can occur at a different time than another. However, the system fails when any device fails (redundancy is being neglected in this case). Therefore, the unreliability function of the three-phase system  $F_{sys}$  can be obtained by,

$$F_{sys}(x) = 1 - \prod_{i=1}^6 (1 - F_i(x)). \quad (27)$$

Due to the uniform power distribution between the inverter phases, all devices converge to the same cumulative density function  $F(x)$ . Then, it is possible to simplify (27) by,

$$F_{sys}(x) = 1 - (1 - F(x))^6. \quad (28)$$

## 5. Lifetime results: case study

The semiconductors power losses were estimated using PLECS environment. Moreover, reliability analysis, including Monte Carlo simulation, was performed on the MATLAB platform.

Fig. 9 shows simulated diode and IGBT switching and conduction power losses for varying  $P$  and  $Q$  injection conditions. As expected, the total power losses are directly affected by the reactive power compensation. According to Fig. 9(a), the diode conduction losses when the PV inverter injects only  $Q$  ( $\theta = \pm 90^\circ$ ) are approximately 5 times higher than the power losses with only  $P$  injection ( $\theta = 0$ ). Fig. 9(d) shows that the IGBT conduction losses behavior is opposite, considering the points analyzed above.

The diode and IGBT switching power losses have the same behavior: they are higher for injections of  $P$  than for injections of  $Q$ , as discussed in Section 2. The combined injection of  $Q$  and  $P$  increases conduction and switching power losses, since it is directly related to the current flowing in the power devices.

Fig. 9(c) and (f) show the total power losses of the diode and IGBT, respectively. For the conditions of  $Q = 8$  kvar and  $P = 8$  kW, the IGBT total power losses are 6 times greater than the diode total power losses,

which causes the extra heating of these components.

Fig. 10(a) and (c) confirm that the reactive power injection increases the mean junction temperature of the IGBT and diode, respectively. In addition,  $\Delta T_j$  is also affected, as shown in Fig. 10(b) and (d) for the IGBT and diode.  $T_{jm}$  and  $\Delta T_j$  for the  $Q$  compensation case are always higher, compared to the case without reactive power compensation. From the results observed in Figs. 9 and 10, the IGBT showed higher power losses, junction temperature and junction temperature fluctuation, compared to the diode. Therefore, the IGBT is expected to be the system critical component. Due to the reasons present above, it was selected to evaluate the system lifetime.

The multifunctional PV inverter components are subject to higher thermal stresses over the traditional PV inverter devices. This extra stress can cause more damage to the power devices and can impact their reliability and lifetime. The one-year thermal loading distribution obtained for the power modules under the mission profile conditions was used as an input to calculate the accumulated damage per year. Three scenarios are evaluated in this analysis:

- Multifunctional operation without reactive power injection (base case);
- Multifunctional operation with reactive power injection (without active and reactive power injection restrictions);
- Multifunctional operation with dynamic power saturation (with active and reactive power injection restrictions).

The results are shown in Table 5. It can be noticed that the reactive power compensation according to the load requirements causes greater damage to the devices (0.1067), when compared to the base case (0.0357). Besides, a damage reduction of 48.4% is observed comparing the results with and without dynamic saturation.

In order to statistically evaluate the reactive power injection impacts on the inverter reliability, Fig. 11 shows the component and system-level unreliability curves. Fig. 11(a) shows the Monte Carlo simulation output distribution in histogram form for the three scenarios described above, where a fit using the Weibull PDF is performed. It is noted that the injection of  $Q$  strongly impacts the IGBT lifetime distribution. With  $Q$  injection, there is a higher concentration of the distribution  $f(x)$  in the range of 10–15 years. On the other hand, without  $Q$

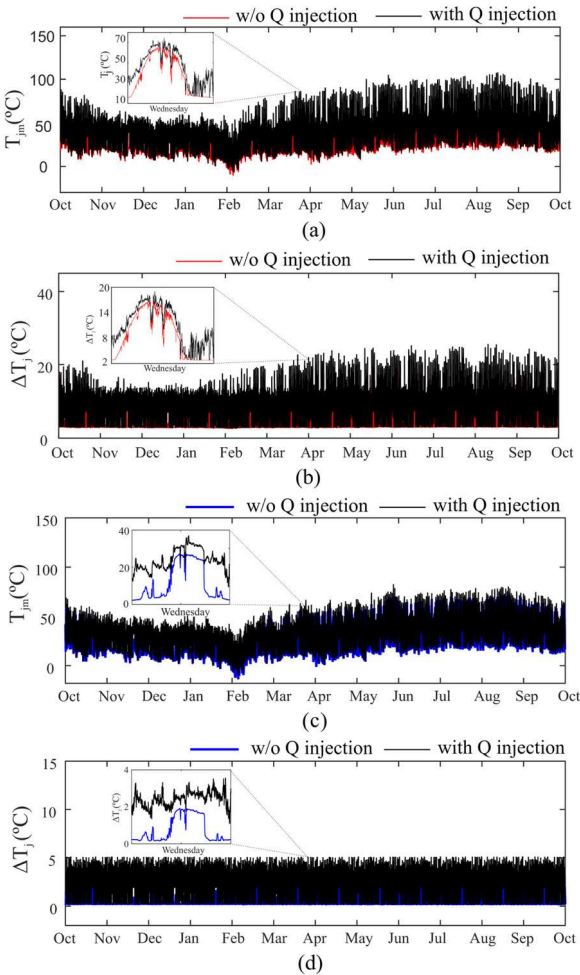


**Fig. 10.** (a) IGBT mean junction temperature behavior with and without  $Q$  injection. (b) IGBT junction temperature fluctuation with and without  $Q$  injection. (c) Diode mean junction temperature behavior with and without  $Q$  injection. (d) Diode junction temperature fluctuation with and without  $Q$  injection.

**Table 5**

Lifetime consumption due to  $T_a$ ,  $G$  and  $Q$  profiles, based on the Palmgren-Miner's rule (22) for one year.

Time constant	Lifetime consumption (LC)		
	w/o $Q$ inj.	with $Q$ inj.	with dyn. sat.
Long-term	$1.76 \times 10^{-7}$	$3.37 \times 10^{-6}$	$1.04 \times 10^{-6}$
Short-term	0.0357	0.1067	0.0551
Total	0.0357	0.1067	0.0551

injection, a considerable distribution is present in the range of 30–40 years. Finally, an intermediate result is obtained considering the dynamic saturation, whose distribution is concentrated within 18–28 years.

The unreliability functions of one component (i.e. component-level) for the scenarios without and with  $Q$  injection and considering the dynamics saturation are indicated in Fig. 11(b). The  $B_{10}$  lifetime of the power device for the first case is 26.1 years. This parameter indicates that 10% of the power devices is expected to fail until 26.1 years. On the other hand, for the second one,  $B_{10}$  lifetime of the power device declined to 8.6 years, which reduces power device lifetime by 67%. Regarding the dynamic saturation, the estimated  $B_{10}$  value decreases to 16.8 years, a reduction of 35.6% compared to the base case.

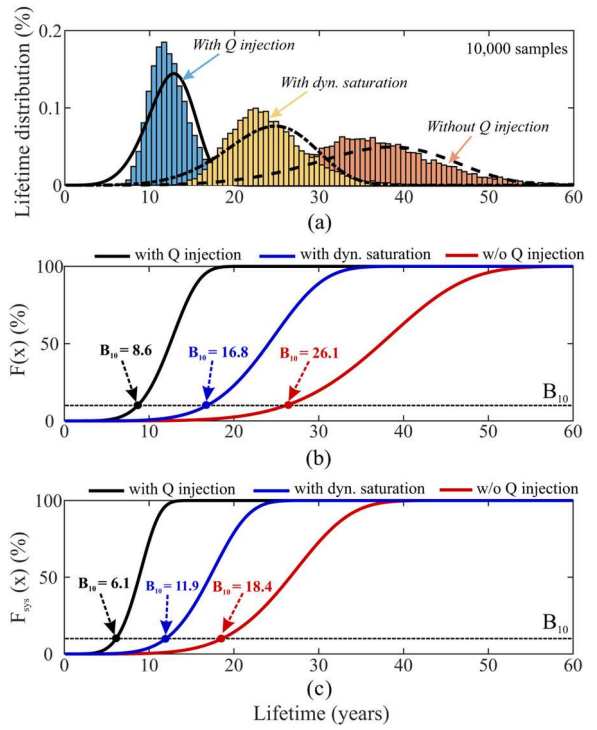


**Fig. 11.** (a) Damage distribution analysis of the power module for the three scenarios defined. Unreliability function of the (b) IGBT component. (c) PV system, considering the three scenarios.

Fig. 11(c) shows the system-level unreliability function for the scenarios without and with  $Q$  injection and considering the dynamics saturation, respectively. The system-level  $B_{10}$  differs significantly from the component-level lifetime, for these cases. The system-level  $B_{10}$  is 18.4 years if the reactive power injection is not considered. Considering it without restrictions, the system-level  $B_{10}$  lifetime declines to 6.1 years. This means that the PV inverter has a lifetime reduction of 66.8% when compared to the base case. Finally, performing the dynamic saturation, a  $B_{10}$  of 11.9 years is observed, about 35.3% smaller compared to the base case lifetime and almost twice the size of the inverter lifetime with total reactive injection.

### 5.1. Final considerations

It is difficult to precisely estimate the lifetime of a power device. It involves several other factors that are beyond the scope of this paper. For example, in the lifetime calculation, only the thermal cycles induced by the mission profile in the range of 1–15 s are considered. Even with high oscillations in min-hour time constants present in the reactive power profile, any long-term cycle outside this range was ignored due to the lifetime model limitation. In order to mitigate these errors, all analyzes were presented using the same methodology, by means of comparison of the estimated system lifetime considering several scenarios.

The inverter is configured to inject reactive power during voltage sag events ranged at sec-min intervals, in order to satisfy the current grid code requirements. In such case, only a control update on the software firmware is required to convert the traditional inverter into a multifunctional inverter with continuous reactive power injection. Unfortunately, a significant reduction in the multifunctional PV inverter reliability is observed when the reactive injection is performed. Hardware upgrade, exchange of power devices based on current oversizing and a physics-of-failure-oriented design are some approaches found in the literature to ensure a highly reliable operation of the PV inverter with reactive power compensation.

## 6. Conclusion

The lifetime impact on a multifunctional PV inverter compensating reactive power was provided in this work. It was verified that the reactive power injection implies in the additional increase in the junction temperature and consequently in the thermal stress of the power devices. Thus, the Monte Carlo analysis reveals that the lifetime consumption of the PV inverters decreases considerably with the reactive power injection. As a result, the total reactive power injection reduced the inverter lifetime by 66.8% compared to the traditional operation. Applying the dynamic power saturation, a lifetime reduction of 35.3% was observed in relation to the base case. Regarding the total and partial reactive power injection, the inverter lifetime almost doubles considering the dynamic power saturation, according to the  $B_{10}$  metric.

The PV inverter with reactive power support can improve the quality of the power system, reduce power losses in the distribution and transmission lines, provide voltage regulation and aids in events such as transient voltage sags. However, despite the great attractiveness of the multifunctional PV inverter, a considerable reduction in the PV inverters lifetime is observed when providing this new functionality. Thus, there is a trade-off between the advantages and impacts of reactive power injection and some obstacles related to the reliability and lifetime of the multifunctional inverter still have to be overcome to make it even more attractive.

## References

- [1] I.E. Agency, Renewables 2018: Market analysis and forecast from 2018 to 2023, (2019) <https://www.iea.org/renewables2018/power/>.
- [2] A. Sangwongwanich, Y. Yang, D. Sera, F. Blaabjerg, Lifetime evaluation of grid-connected PV inverters considering panel degradation rates and installation sites, *IEEE Trans. Power Electron.* 33 (2) (2018) 1225–1236.
- [3] E.G. de Andrade, H.A. de Oliveira, W.V. Ribeiro, R.C. de Barros, H.A. Pereira, A.F. Cupertino, Power losses in photovoltaic inverter components due to reactive power injection, *INDUSCON* (2016) 1–7.
- [4] A. Anurag, Y. Yang, F. Blaabjerg, Thermal performance and reliability analysis of single-phase PV inverters with reactive power injection outside feed-in operating hours, *IEEE J. Emerg. Sel. Topics Power Electron.* 3 (4) (2015) 870–880.
- [5] W. Libo, Z. Zhengming, L. Jianzheng, A single-stage three-phase grid-connected photovoltaic system with modified MPPT method and reactive power compensation, *IEEE Trans. Energy Convers.* 22 (4) (2007) 881–886.
- [6] P. Reigosa, Smart derating of switching devices for designing more reliable PV inverters, Aalborg University, 2014 Master's thesis.
- [7] A. Pinto, R. Zilles, Reactive power excess charging in grid-connected PV systems in Brazil, *Renew. Energy* 62 (2014) 47–52.
- [8] M.N.I. Sarkar, L.G. Meegahapola, M. Datta, Reactive power management in renewable rich power grids: a review of grid-codes, renewable generators, support devices, control strategies and optimization algorithms, *IEEE Access* (2018) 41458–41489, <https://doi.org/10.1109/ACCESS.2018.2838563>.
- [9] L. Liu, H. Li, Y. Xue, W. Liu, Reactive power compensation and optimization strategy for grid-interactive cascaded photovoltaic systems, *IEEE Trans. Power Electron.* 30 (1) (2015) 188–202.
- [10] A. Golnas, PV system reliability: an operator's perspective, *IEEE J. Photovolt.* 3 (1) (2013) 416–421.
- [11] V.N. Ferreira, A.F. Cupertino, J. Brito, B.J.C. Filho, IGBT power modules lifetime in 2-level PV-inverters under harsh environmental conditions, *IEEE PEDG* (2017) 1–7.
- [12] J. Zhang, H. Wang, X. Cai, S. Igarashi, Y. Li, Z. Wang, Thermal control method based on reactive circulating current for anti-condensation of wind power converter under wind speed variations, *IEEE PEAC* (2014) 152–156.
- [13] O. Gandhi, C.D. Rodriguez-Gallegos, N.B. Gorla, M. Bieri, T. Reindl, D. Srinivasan, Reactive power cost from PV inverters considering inverter lifetime assessment, *IEEE Trans. Sustain. Energy* 10 (2) (2019) 738–747.
- [14] A. Sangwongwanich, E. Liivik, F. Blaabjerg, Photovoltaic module characteristic influence on reliability of micro-inverters, *IEEE CPE-POWERENG* (2018) 1–6.
- [15] A. Anurag, Y. Yang, F. Blaabjerg, Reliability analysis of single-phase PV inverters with reactive power injection at night considering mission profiles, 2015 IEEE Energy Conversion Congress and Exposition (ECCE) (2015) 2132–2139.
- [16] Z. Zou, Z. Wang, M. Cheng, Modeling, analysis, and design of multifunction grid-interfaced inverters with output LCL filter, *IEEE Trans. Power Electron.* 29 (7) (2014) 3830–3839.
- [17] L.S. Xavier, A.F. Cupertino, H.A. Pereira, Ancillary services provided by photovoltaic inverters: single and three phase control strategies, *Comput. Electr. Eng.* (2018).
- [18] S. Golestan, J.M. Guerrero, J.C. Vasquez, Three-phase PLLs: a review of recent advances, *IEEE Trans. Power Electron.* 32 (3) (2017) 1894–1907.
- [19] F. Casanellas, Losses in PWM inverters using IGBTs, *IEE Proc. - Elec. Power Appl.* 141 (5) (1994) 235–239.
- [20] M.H. Bierhoff, F.W. Fuchs, Semiconductor losses in voltage source and current source IGBT converters based on analytical derivation, *IEEE PESC*, vol. 4 (2004) 2836–2842.
- [21] Y. Xiong, X. Cheng, Z.J. Shen, C. Mi, H. Wu, V.K. Garg, Prognostic and warning system for power-electronic modules in electric, hybrid electric, and fuel-cell vehicles, *IEEE Trans. Ind. Electron.* 55 (6) (2008) 2268–2276.
- [22] H. Wang, M. Liserre, F. Blaabjerg, P. de Place Rimmen, J.B. Jacobsen, T. Kvisgaard, J. Landkildehus, Transitioning to physics-of-failure as a reliability driver in power electronics, *IEEE J. Emerg. Sel. Topics Power Electron.* 2 (1) (2014) 97–114.
- [23] K. Ma, M. Liserre, F. Blaabjerg, T. Kerekes, Thermal loading and lifetime estimation for power device considering mission profiles in wind power converter, *IEEE Trans. Power Electron.* 30 (2) (2015) 590–602.
- [24] K. Ma, F. Blaabjerg, Reliability-cost models for the power switching devices of wind power converters, *IEEE PEDG* (2012) 820–827.
- [25] Y. Yang, A. Sangwongwanich, F. Blaabjerg, Design for reliability of power electronics for grid-connected photovoltaic systems, *CPSS Trans. Power Electron. Appl.* 1 (1) (2016) 92–103.
- [26] M.G. Villalva, J.R. Gazoli, E.R. Filho, Comprehensive approach to modeling and simulation of photovoltaic arrays, *IEEE Trans. Power Electron.* 24 (5) (2009) 1198–1208.
- [27] R. Bayerer, T. Herrmann, T. Licht, J. Lutz, M. Feller, Model for power cycling lifetime of IGBT modules – various factors influencing lifetime, *CIPS* (2008) 1–6.
- [28] I. Technologies, Technical information IGBT modules. URL [http://song-shan.com/en/upload/file/20140413/122019\\_Use%20of%20Power%20Cycling%20Curves%20for%20IGBT4%20.pdf](http://song-shan.com/en/upload/file/20140413/122019_Use%20of%20Power%20Cycling%20Curves%20for%20IGBT4%20.pdf).
- [29] Y. Shen, H. Wang, Y. Yang, P.D. Reigosa, F. Blaabjerg, Mission profile based sizing of IGBT chip area for PV inverter applications, *IEEE PEDG* (2016) 1–8.
- [30] P.D. Reigosa, H. Wang, Y. Yang, F. Blaabjerg, Prediction of bond wire fatigue of IGBTs in a PV inverter under a long-term operation, *IEEE Trans. Power Electron.* 31 (10) (2016) 7171–7182.
- [31] D. Zhou, H. Wang, F. Blaabjerg, S.K. Koer, D. Blom-Hansen, System-level reliability assessment of power stage in fuel cell application, *IEEE ECCE* (2016) 1–8.